Impact of Temperature on Zeolitization Elucidated by *In-Situ* High-Energy X-ray Total Scattering Measurement

Zimu Zhou[1], Peidong Hu[1, 2], Hiroki Yamada[3, 4], Jo-Chi Tseng[3], Koji Ohara[3, 4], Yasuo Yonezawa[2], Tatsuya Okubo[1], Toru Wakihara[*1, 2]

[1] *Department of Chemical System Engineering, The University of Tokyo, 7-3-1 Hongo, Bunkyo-ku, Tokyo 113-8656, Japan*

[2] *Institute of Engineering Innovation, The University of Tokyo, 2-11-16 Yayoi, Bunkyo-ku, Tokyo 113-8656, Japan*

[3] *Japan Synchrotron Radiation Research Institute/SPring-8, 1-1-1 Kouto, Sayo-cho, Sayo-gun, Hyogo 679-5198, Japan*

[4] *Faculty of Materials for Energy, Shimane University, 1060 Nishi-Kawatsu-Cho, Matsue, Shimane 690-8504, Japan*

* Corresponding author:

Prof. Toru Wakihara

Tel: +81-3-5841-3821

E-mail: wakihara@chemsys.t.u-tokyo.ac.jp

ABSTRACT

Zeolites are generally synthesized by the hydrothermal method, where temperature is an important parameter. Previous studies have shown that aging can accelerate the synthesis of zeolites; however, while the phenomena have been well investigated, medium-range structural evolution of the aluminosilicate species during the zeolite synthesis has not been fully understood yet, leaving the underlying mechanism unclear. Herein, zeolite X (FAU-type framework) is selected as an example to reveal the role of temperature in zeolitization, and the structural evolutions during the induction and crystallization process of zeolite X under different temperatures are comparatively investigated by the advanced *in-situ* high-energy X-ray total scattering (HEXTS) technique, combined with UV-Raman spectroscopy and *ex-situ* HEXTS. Zeolite X is synthesized in a home-made reactor, by aging the reactants at 70 °C prior to the hydrothermally treatment at 90 °C. At an aging temperature of 70 °C, 4-rings (4Rs) and double 6-ring (*d6r*) units are formed in the amorphous matrix, which are subsequently assembled to form ordered large structures (12Rs and *sod*-cages) at 90 °C, triggering the formation of a crystalline framework. In comparison, when the reactant is only treated at 90 °C without aging, an SOD-type framework is formed instead of the targeted FAU-type due to the lack of *d6r* units. Our findings demonstrate that a suitable aging temperature is crucial for zeolite synthesis, and temperature significantly influences the local structural evolutions during the formation of zeolites.

1. INTRODUCTION

Zeolites are microporous materials constructed from the three-dimensional connection of TO_4 (T = Si, Al, etc.) tetrahedra [1]. Owing to the large specific surface area, uniform microporosity, solid acidity and ion exchange capacity, zeolites have been widely applied as catalysts, adsorbents, and ion-exchangers in chemical industry as well as emerging applications such as exhaust gas treatment, biomass conversion and carbon capture in sustainable chemistry [2]. Zeolites can be artificially synthesized from Si and Al sources, water, mineralizers, and structure-directing agents in batch systems under hydrothermal conditions. To fulfill the increasing industrial demands, rational synthesis of zeolites with controllable crystallization process is considered crucially important. However, the crystallization mechanism of zeolites is still a black box, due to the complexity of zeolite formation process which cannot be simply explained by the classical nucleation and crystal growth models following a monomer-to-cluster pathway [3]. Instead of monomers, a vast number of species may be present in the synthesis mixtures during the zeolite formation process, including nanocrystals, colloids, amorphous nanoparticles, gel-like islands, oligomers, etc. [4]. The ubiquitous presence of amorphous intermediates throughout crystallization makes zeolites quintessential examples of materials that are crystallized via non-classical mechanisms. It is generally considered that during the crystallization process of zeolites, a primary amorphous material is formed after the initial reactants are mixed with each other. After a period of time, the primary amorphous material is converted into the secondary amorphous material, which is a pseudo-steady-state intermediate due to the equilibration reactions [5]. In the final stage of the synthesis (usually at an elevated temperature for a prolonged period), the secondary amorphous material is converted into the crystalline zeolite product. Understanding of such non-classical mechanisms, however, is still limited because of the inadequate analytical techniques available to observe the dynamic processes with sufficient spatiotemporal resolution [6].

Among the various synthetic parameters, temperature is a crucial factor in the hydrothermal synthesis of zeolites. Zeolite crystallization typically occurs between 70 °C and 200 °C. Temperatures lower than 70 °C are likely to produce amorphous products, while temperatures above 200 °C can lead to the formation of non-zeolitic dense phases [7]. Generally, a targeted zeolite phase can only be formed within a certain range of

temperature, and the temperature has a phase-selective effect even with the same composition of the reactants, such as the phase selection between sodalite (SOD) and zeolite A (LTA), zeolite P (GIS) and zeolite X (FAU), and ZSM-5 (MFI) and mordenite (MOR) [8,9]. Aging is necessary for the synthesis of some zeolites such as zeolite Y (FAU) [10], and the temperature of aging also significantly influences the outcome of synthesis [11]. It has been reported that elevating the aging temperature to 90 °C enables the ultrafast synthesis of AFX-type zeolite, while a lower aging temperature at 25 °C results in the formation of ANA-type zeolite with a slower crystallization rate [12]. Temperature not only affects the phase of the product, but also the nucleation and crystal growth pathways. An increase in the hydrothermal temperature typically results in both accelerated nucleation and crystal growth, as previously reported by the increased crystal growth rate of zeolite X (FAU) with the temperature [13,14]. Besides, it is indicated by atomic force microscopy (AFM) that the crystal growth pathways of zeolite W (MER) might vary with the synthesis temperature [15]. These above-mentioned studies have cast light on the phase-selective effect, as well as effects of temperature on the crystal growth pathways at a meso-scale. However, so far, the effects of temperature on the medium-range structural evolutions—typically involving the secondary building units (SBUs) such as rings, structural units, and cages at a scale of 5-20 Å [16]—are still unclear, due to the complexity of disorder-to-order transition of zeolites and the incapability of characterizing the local structures in an amorphous matrix.

Spectroscopic techniques, such as Fourier-transform infrared (FT-IR) spectroscopy, Raman spectroscopy, and magic-angle spinning nuclear magnetic resonance (MAS NMR) spectroscopy can be applied to observe the changes in chemical bonds and ring structures during the formation of zeolites [17–20]. However, spectroscopic method alone is insufficient to gain conclusive insights into the local structures of the amorphous precursors. In addition to the spectroscopic methods, pair distribution function (PDF) analysis is considered as a powerful tool for probing the atomic-scale to intermediate-range structures of materials including liquids, polymers, glasses, ceramics, and zeolites [21–25]. To obtain scattering data for PDF analysis, high-energy X-ray total scattering (HEXTS) measurement is usually performed using a synchrotron X-ray with a high spatial resolution [26,27]. Our early work combining *ex-situ* HEXTS and reverse Monte Carlo (RMC) [28] methods indicates that even numbered rings such as 4Rs and 6Rs already exist in the amorphous aluminosilicate

precursors [29]. The abundance of 4Rs in the amorphous precursors is also evidenced by the UV-Raman spectra results [30]. However, the above methods cannot provide a clear pattern of the relative changes in the local structures with the time, and the impact of temperature on the formation of ordered structures has not been elucidated. As shown in our recent work, *in-situ* HEXTS has the following advantages over the *ex-situ* method: (1) preserving the rudimentary structures of the amorphous precursors that may be altered by the post-treatments such as quenching and drying; (2) capability of observing the dynamic processes with a sufficient time resolution; (3) ability to discern the minor structural changes by relative PDF analysis [31,32]. A combination of the techniques mentioned above, including the spectroscopic methods, *ex-situ* HEXTS and *in-situ* HEXTS, is expected to be promising for investigating the local structural evolutions of amorphous zeolite precursors towards the crystalline products during the hydrothermal synthesis.

Zeolite X is an FAU-type zeolite with a Si/Al ratio lower than 1.5, which has been widely applied in chemical industry such as the selective adsorption of CO_2 from the gas streams, the pre-purification of air, and the industrial air separation [33]. A previous work has comparatively investigated the crystallization behavior of zeolite X (FAU) in a silicate solution system and in a fumed silica system [30], demonstrating that the different reactant systems kinetically affect the formation of short-range order, thus changing the nucleation rates and crystal sizes. However, in either system the synthesis of zeolite X is conducted at the same temperature of 80 °C, which does not include information regarding the effects of temperature on the crystallization pathway. In terms of the temperature-related effects, it has been reported that zeolite X can be synthesized at 80 °C, while amorphous product is formed at temperatures below 70 °C, and undesired phases such as zeolite P (GIS) and sodalite (SOD) are formed at higher temperatures ranging from 90 °C to 200 °C [34]. But the evolutions of short-to-medium-range order during the crystallization of zeolite X are beyond the scope of the above study [34]. A rationally controlled aging process prior to crystallization could also play a critical role in the formation of FAU-type zeolite, where an optimal aging time of 2 days at room temperature yields pure FAU with high crystallinity [35]. ^{29}Si MAS NMR further shows the effects of aging on the short-range order in the solid products, especially changes in the distribution of Al. However, the previous study has mainly focused on aging for different periods at room temperature, without exploring the effects of varying aging temperatures

[35].

In this work, the effect of temperature on the formation mechanism of zeolite X was comprehensively investigated using a combination of *in-situ* HEXTS–PDF analysis, and other characterization techniques such as *ex-situ* HEXTS and UV-Raman spectroscopy. The use of a home-made *in-situ* reactor allows real-time tracking of structural evolution during both the induction and crystallization stages. Pure zeolite X is synthesized by aging the precursor at 70 °C for 2.5 h followed by a hydrothermal treatment at 90 °C for 2.5 h. It is shown that at 70 °C, 4Rs and *d6r* units are significantly formed in the amorphous matrix. These medium-range structural units subsequently assemble into larger ordered structures (12Rs and *sod*-cages) during hydrothermal treatment at 90 °C, enabling crystallization of the FAU-type framework. In comparison, direct treatment at 90 °C for 5 h without aging leads to the formation of an alternative SOD-type framework without *d6r*, highlighting the role of pre-formed *d6r* units in phase selection and suggesting that a proper aging temperature (70 °C) is important for the formation of zeolite X. Our findings clearly demonstrate how temperature controls the evolution of medium-range structures in and provide mechanistic insight for zeolite synthesis with rational control.

2. EXPERIMENTAL SECTION

2.1. Materials. Colloidal silica (LUDOX HS-40, Sigma-Aldrich), sodium aluminate (Al/NaOH = 0.79, FUJIFILM Wako Pure Chemical Corporation), potassium hydroxide solution ($KOH_{(aq)}$, 50 wt % in water, FUJIFILM Wako Pure Chemical Corporation), and sodium hydroxide solution ($NaOH_{(aq)}$, 50 wt % in water, FUJIFILM Wako Pure Chemical Corporation) were used.

2.2. Synthesis of Zeolite X and Precursors. The reactant mixture of zeolite X was prepared with the molar composition of $2.93Na_2O$: $0.88K_2O$: $0.35Al_2O_3$: $1SiO_2$: $50H_2O$. A transparent Al-containing alkaline solution ($2.93Na_2O$: $0.88K_2O$: $0.35Al_2O_3$: $50H_2O$) was prepared by adding the sodium aluminate to a mixture of $NaOH_{(aq)}$, $KOH_{(aq)}$, and deionized water, followed by the agitation at a rate of 400 rpm for 10 min using a magnetic stirrer. Then, colloidal silica was added dropwise to the Al-containing solution under continuous stirring at 400 rpm for 10 min to obtain a milky white mixture. Approximately 5 g of the reactant mixture was

transferred to a homemade hydrothermal reactor system (capacity: ca. 10 mL, Fig. S1a) and then subjected to a programmed hydrothermal treatment. Fully crystalline zeolite X was synthesized via a three-step hydrothermal program, with an agitation rate of 30 times/min and an initial air pressure of 0.25MPa: the reactant mixture was first kept at 30 °C for ca. 1800 s (30 min), followed by an aging process at 70 °C for ca. 9000 s (2.5 h), and in the final step the temperature was raised to 90 °C and kept constant for ca. 9000 s (2.5 h). After the synthesis, the as-obtained product was cooled down to ambient temperature by flowing air and was subjected to centrifugation (14000 rpm × 5 min) to separate the solid and liquid phases. The liquid phase was collected and diluted 5000 times for elemental analysis. The solid product was recovered by filtration, thoroughly washed with deionized water until the pH value of the filtrate became close to neutral, and dried overnight at 80 °C. Similarly, amorphous and partially crystalline precursors of zeolite X were also prepared using the above method with varying temperature profiles.

2.3. Characterizations. The powder X-ray diffraction (XRD) patterns of the solid products were collected using a Rigaku Ultima IV X-ray diffractometer (Cu Kα radiation source, λ = 0.15406 nm) at 40 kV, 40 mA with a scanning range of 2θ = 3°–50° and a scanning speed of 10° min^{-1}. The relative crystallinity of the products was calculated based on the peak area of the selected Bragg peaks between 20° and 35° (2θ). The sample which was aged under 70 °C for 2.5 h and hydrothermally under 90 °C treated for 16 h was used as the reference for 100% crystallinity. The chemical compositions of the liquid phase and the solid product were determined by inductively coupled plasma-atomic emission spectroscopy (ICP-AES) using a Shimadzu ICPE-9820 spectrometer. The morphology of the solid products was observed using a JEOL JSM-7000F field emission scanning electron microscope (FE-SEM) under an accelerating voltage of 15.0 kV. The ultraviolet (UV)-Raman spectra of the solid samples were measured by a LabRAM Odyssey UV-Raman microscope (HORIBA) with an excitation wavelength of 325 nm. Solid-state magic-angle spinning nuclear magnetic resonance (MAS NMR) measurement for ^{27}Al nuclei was conducted using a JEOL ECA-500 spectrometer. The ^{27}Al MAS NMR spectra were obtained at a resonance frequency of 130.33 MHz with a π/2 pulse width of 3.2 μs, a relaxation delay of 5 s, and a spinning frequency of 14 kHz.

2.4. *Ex-situ* and *In-situ* HEXTS Measurements and PDF Analysis. The *ex-situ* HEXTS measurements

on the solid products were conducted on the BL04B2 synchrotron XRD beamline at SPring-8, Japan (incident beam energy E = 61.339 keV, wavelength λ = 0.2021 Å) with a horizontal two-axis diffractometer. The powder samples (ca. 0.1 g) were held in Kapton® glass capillaries with a diameter of 1.0 mm, and exposed to the synchrotron X-ray radiation for 10 min under ambient temperature and vacuum conditions. The maximum scattering vector Q ($Q = 4\pi\sin\theta/\lambda$) for the *ex-situ* HEXTS measurement was 25.7 Å^{-1}. The *in-situ* HEXTS measurements were performed on the BL08W high-energy XRD beamline at SPring-8, Japan (E = 114.13 keV, λ = 0.1086 Å), equipped with a PerkinElmer XRD 1621 CN3 flat-panel detector. The homemade reactor was fixed in the beamline, and the position of the synchrotron X-ray beam was adjusted to pass through the glass sample vial. The optical setups were calibrated as described in the previous study [31]. The scattering data was recorded at intervals of 30 s, by averaging 30 frames of the imaging data collected for an exposure time of 1.0 s per frame. The maximum Q was set to be 21.0 Å^{-1}.

Obtained X-ray total scattering data went through well-established analytic procedures including absorption, background, Compton scattering corrections, followed by normalization to obtain Faber-Ziman total structure factor, $S(Q)$. The obtained $S(Q)$ went through Fourier transformation to give a real-space PDF expressed as the Eq. (1) [29]:

$$G(r) = \frac{2}{\pi}\int_{Q_{\min}}^{Q_{\max}} Q[S(Q) - 1]\sin(Qr)\,\mathrm{d}Q \tag{1}$$

$G(r)$ describes the probability of finding two atoms from a certain distance r in the system, which can be further interpretated to solve the local atomic arrangements of disordered materials. In the *in-situ* HEXTS measurements, the relative PDF, d$G(r)$, was further calculated according to the following Eq. (2) and Eq. (3) [36]:

$$\mathrm{d}G(r) = \frac{2}{\pi}\int_{Q_{\min}}^{Q_{\max}} \Delta F(Q)\sin(Qr)\,\mathrm{d}Q \tag{2}$$

$$\Delta F(Q) = \frac{Q\Delta I_{\mathrm{tot}}}{N\langle f(Q)\rangle^2} \tag{3}$$

where $\langle f(Q)\rangle$ represents the sum of atomic form factors, N represents the number of scattering atoms, and ΔI_{tot} is the difference between the scattering data of the sample and the reference. d$G(r)$ is calculated as the Fourier transform of the difference in total structure factor $\Delta F(Q)$ between a time-evolving sample and the reference

sample. Since N and $\langle f(Q)\rangle$ are constants for a given system, the essential definition of the relative PDF d$G(r)$ lies in the difference of raw scattering intensities, $\Delta I_{tot}(Q)$, showing how the local structures evolve relative to the reference state. The subtraction $I_1(Q)$- $I_0(Q)$ is performed in the Q-space prior to Fourier transformation, rather than in the real-space. This ensures that the calculated d$G(r)$ represents only the evolving interatomic correlations, while contributions from the background signals and the unchanged structures are effectively removed [36].

In this work, for each temperature (30 °C/70 °C/90 °C) during the heating program, the first scattering data after reaching the designated temperature was selected as the reference. The reference was adjusted for each temperature due to changes in water density with the temperature. Before the calculation of PDFs, the scattering due to the glass sample vial was subtracted from all the total scattering data. The calculated d$G(r)$ patterns thus sensitively capture the development of short-range to medium-range structures—such as 4Rs, 6Rs, and *d6r* units—prior to the formation of a long-range order.

3. RESULTS

3.1 *Ex-situ* Characterizations. The syntheses were performed using the homemade reactor for the *in-situ* HEXTS measurement (Fig. S1), according to the temperature profile shown in Fig. 1a. Colloidal silica and sodium aluminate were used as the Si and Al sources, respectively. Throughout the synthesis, the reactant mixture was well mixed by agitating at a rate of 30 rpm. The relative crystallinity of the solid product and the Si/Al ratio throughout the synthesis are listed in Table S1. As shown in the XRD patterns (Fig. 1b), no zeolitic structure is formed during the aging period at 30 °C for 30 min and subsequently at 70 °C for 2.5 h. After 2.5 h at 70 °C, several diffraction peaks could be observed in the range of 22°–45°, which are not zeolitic products but considered to be derived from aluminum hydroxide species. At this stage, the center of the amorphous silica band shifts from 27.8° to 29.5°, suggesting a decrease in the average interatomic distances, presumably due to the formation of an increasingly compact structure in the amorphous aluminosilicate matrix [37]. Diffraction peaks of the FAU phase start to appear after the reactant is hydrothermally treated at 90 °C for 0.5 h, and the fully crystallized FAU-type zeolite can be obtained after the hydrothermal synthesis time at 90 °C

is extended to 2.5 h. Elemental analysis via ICP-AES (Fig. 1c) shows that in the initial (0 h) solid product is mainly composed of amorphous silica, with the majority of the Al species remaining in the solution phase. During the agitation under 30 °C, the Al species are incorporated into the amorphous silica framework, evidenced by the drastic increase in the percentage of Al in the solid product (Fig. 1c). After the reactants are treated under 70 °C for 30 min, 99% of Al has been incorporated into the amorphous solid network to form an amorphous aluminosilicate precursor. Meanwhile, a decrease in the fraction of Si in the solid product suggests the release of Si atoms into the liquid phase, possibly due to the depolymerization of the silica source. From this point forward, the fraction of Si and Al in the solid product remains stable (Fig. 1b), suggesting the formation of a primary amorphous material [5]. As the synthesis proceeds to the stage of hydrothermal treatment under 90 °C, the relative crystallinity of the solid product starts to increase (Fig. 1d), while the elemental compositions of both solid and liquid phases remain stable, with ca. 1% of Al and ca. 33-38% of Si species existing in the liquid phase. The changes in crystal morphology are observed by the scanning electron microscopy (SEM) (Fig. S2). By the end of the hydrothermal synthesis, uniformly-sized crystals with an octahedral shape and a size of ca. 3 μm are formed (Fig. S2f), verifying the formation of well-crystalline zeolite X.

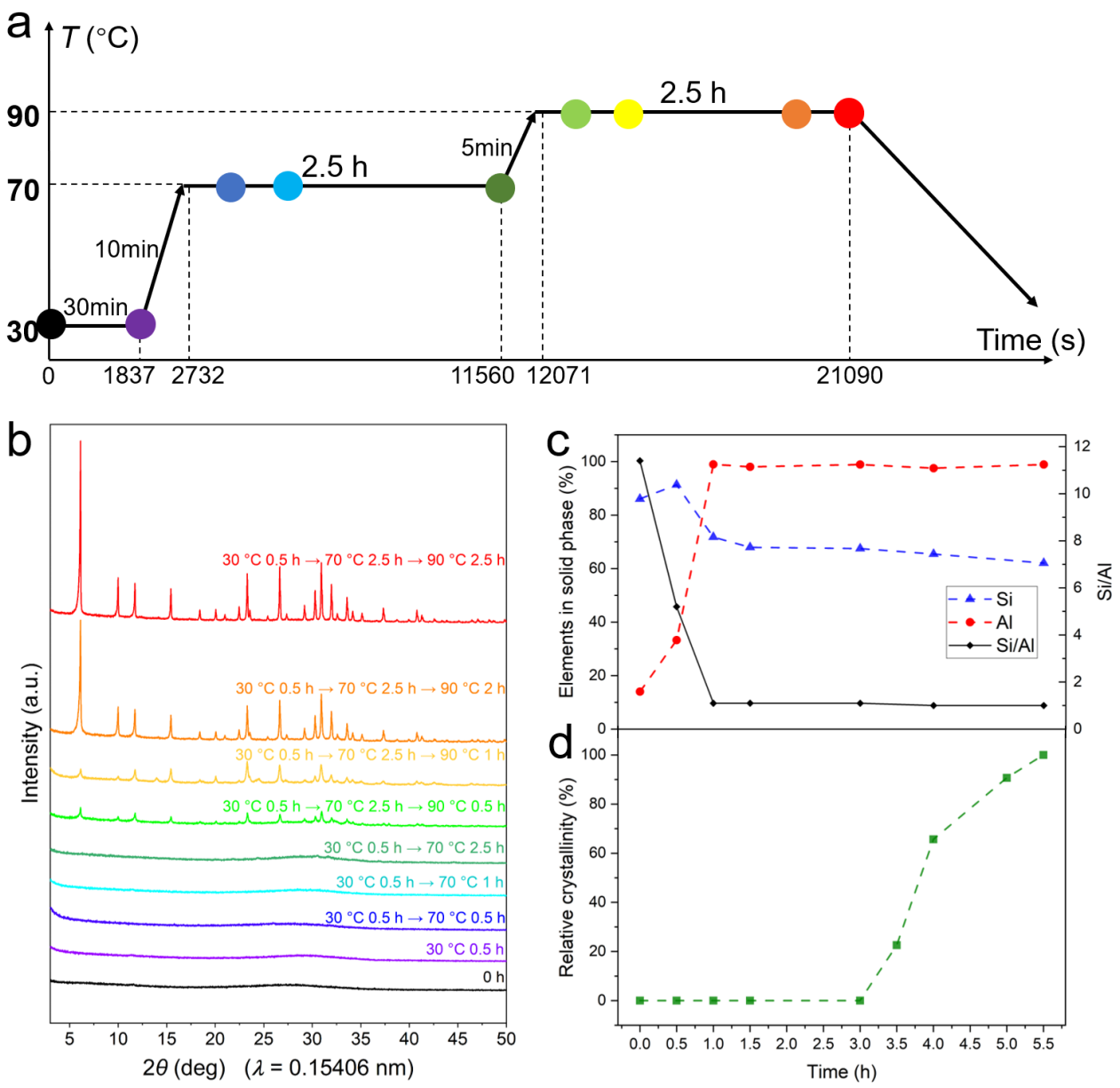

Fig. 1. *Ex-situ* characterizations of the solid products collected throughout the formation process of zeolite X. (a) Temperature profile of the hydrothermal synthesis conducted in the homemade reactor. (b) Powder X-ray diffraction (XRD) patterns. The colors of the XRD patterns are in accordance with the points in the temperature profile. (c) Si/Al ratios in the solid product, and the molar percentages of the elements in the solid product relative to the whole system. (d) Crystallization curve of zeolite X.

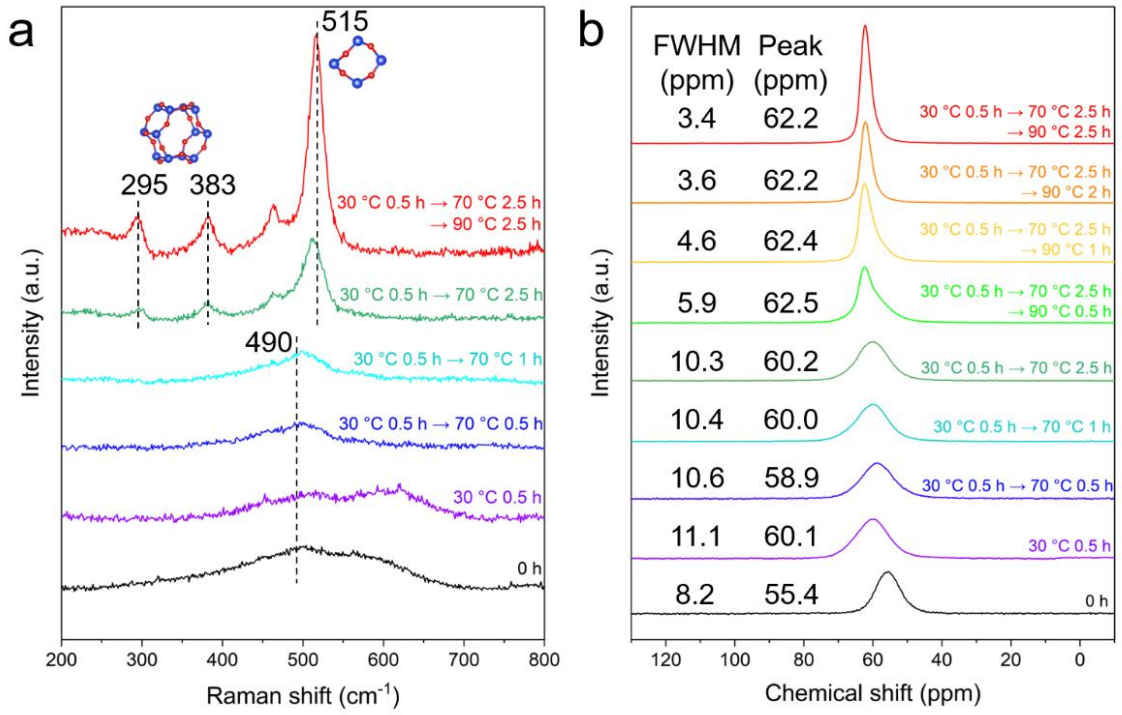

Fig. 2. (a) UV-Raman spectra of the solid products collected throughout the formation process of zeolite X. (b) ^{27}Al MAS NMR spectra of the as-collected solid products.

Changes in the short-range order during the formation of zeolite X are investigated by *ex-situ* UV-Raman spectroscopy (Fig. 2a), which is capable of showing the ring structures in the zeolite framework [38]. For zeolite X with an FAU-type framework, Raman shifts at ca. 515 cm^{-1} are typical of the vibration of 4-rings (4Rs), and the double peaks at 295 and 383 cm^{-1} can be attributed to the *d6r* units [17,18]. ^{27}Al MAS NMR spectra (Fig. 2b) provide complementary information regarding the local structure and chemical environment of Al in the network. The initial solid product at 0 h (Fig. 2a, 0 h) shows a broad Raman band at approximately 350−650 cm^{-1}, and the center of the band is located in the 4R-region (ca. 490 cm^{-1}), suggesting that 4Rs and other larger ring structures are originally included in the amorphous solid (basically the colloidal silica source), among which the 6Rs might exist in abundance, as reported in the previous studies [18]. ^{27}Al NMR spectrum of the same sample (Fig. 2b, 0 h) shows that the Al atoms are already tetrahedrally coordinated in the initial solid product, evidenced by the peak centered at ca. 55.4 ppm and the absence of signal near 0 ppm [39]. During the heating treatment under 30 °C and the first 1 h under 70 °C, in spite of the slight changes in the relative

intensities and shapes of the Raman band, the center of the Raman band remains at a similar position of 490 cm^{-1} (Fig. 2a, 30 °C 0.5 h to 70 °C 1 h). Meanwhile, peak center in the ^{27}Al NMR spectra (Fig. 2b, 0 h and 30 °C 0.5 h) significantly shifts from 55.4 to 60.1 ppm during the 30 °C stage, indicating a decrease in the average T–O–T angle which is presumably due to the formation of Si–O–Al bonds [30]. Combined with the elemental analysis (Fig. 1c), the formation of Si–O–Al structure at 30 °C is presumably due to the incorporation of Al into the amorphous silica network and probably triggers the subsequent formation of Al-rich rings. By the end of the 70 °C stage (Fig. 2a, 70 °C 2.5 h), the formation of well-defined 4Rs is indicated by the shift of Raman peak from ca. 490 cm^{-1} to 512 cm^{-1}, and the formation of *d6r* units is implied by the enhanced Raman signals at 295 and 383 cm^{-1}. Nevertheless, it is noteworthy that more changes in the local structures might have occurred during the aging stage, while the low intensities of the Raman signals, due to the low crystallinity of the solid products, make these changes indiscernible from the Raman spectra. Full width half-maximum (FWHM) of the NMR peaks decreases from 11.1 to 10.3 ppm during the 70 °C stage (Fig. 2b, 30 °C 0.5 h to 70 °C 2.5 h), suggesting that the amorphous aluminosilicate framework becomes increasingly ordered at 70 °C. However, the NMR data does not provide sufficient details to reveal this structural ordering process. After the hydrothermal treatment under 90 °C for 2.5 h, significantly enhanced sharp peaks of 4Rs (515 cm^{-1}) and *d6r* units appear in the UV-Raman spectra (Fig. 2a, 90 °C 2.5 h), which are typical fingerprints of the crystalline zeolite X. ^{27}Al NMR spectra also indicate the formation of crystalline phase at 90 °C (Fig. 2b, 70 °C 2.5 h to 90 °C 2.5 h), evidenced by a significant decrease in the FWHM (from 10.3 to 3.4 ppm) and an increase in the chemical shift (from 60.2 to 62.2 ppm).

3.2. *Ex-situ* and *In-situ* HEXTS Measurements and PDF Analysis. The local structures of the fully-crystalline zeolite X and its amorphous precursors are further characterized by an *ex-situ* HEXTS−PDF analysis (Fig. 3a). The topological structure of FAU-type zeolite framework and its ring structures and structural units are illustrated in Fig. 3b. The interatomic correlations and their corresponding interatomic distances are summarized in Table S2 [40]. The three eminent peaks at 1.6, 2.6, and 3.1 Å are attributed to the first-neighboring T–O, O–O, and T–T correlations, respectively. The T−O 2^{nd} correlation in the 4Rs appears at ca. 3.7 Å, while the T−O 2^{nd} correlation in the 6Rs is located at both ca. 3.9 Å and ca. 4.4 Å, with that in the

12Rs located at ca. 4.4 Å. From the *ex-situ* HEXTS-PDF patterns, the existence of even numbered rings (4Rs and 6Rs) in the aluminosilicate precursor formed after 30 min at 70 °C can be observed, which is in accordance with previous reports [29,30]. The peak at 3.7 Å becomes increasingly pronounced and ordered throughout the formation process of zeolite X, indicating the continuous formation of 4Rs during the zeolite formation process. Clear information of the ring structures, however, cannot be obtained from the peaks at ca. 3.9 Å and 4.4 Å, due to the overlap of signals which could be assigned to various possible structures including the T−T 2nd correlation in the 4Rs/*d6r* units, or the T−O 2nd correlation in the 6Rs/*d6r* units. The peak at ca. 5.1 Å can be exclusively attributed to the T−O 3rd correlation in the 6Rs, which already exist in the initial silica source (0 h) and decrease during the aging period. The signal at ca. 6.9 Å is assigned to the T−O 4th correlation in the *d6r* units, which becomes increasingly pronounced at the aging stage and appears as a clear peak in the final crystalline product. The two peaks at ca. 8.5 Å and 9.4 Å are fingerprints of the *sod*-cages, owing to the T−O 5th correlation and the T−O 6th correlation/ T−T 5th correlation, respectively. Additionally, the peak centered at 11.4 Å can be assigned to the T−O 6th, T−T 5th, and T−T 6th correlations in the 12Rs. The existence of *sod*-cages and 12Rs in the crystalline product confirms its fully ordered framework structure.

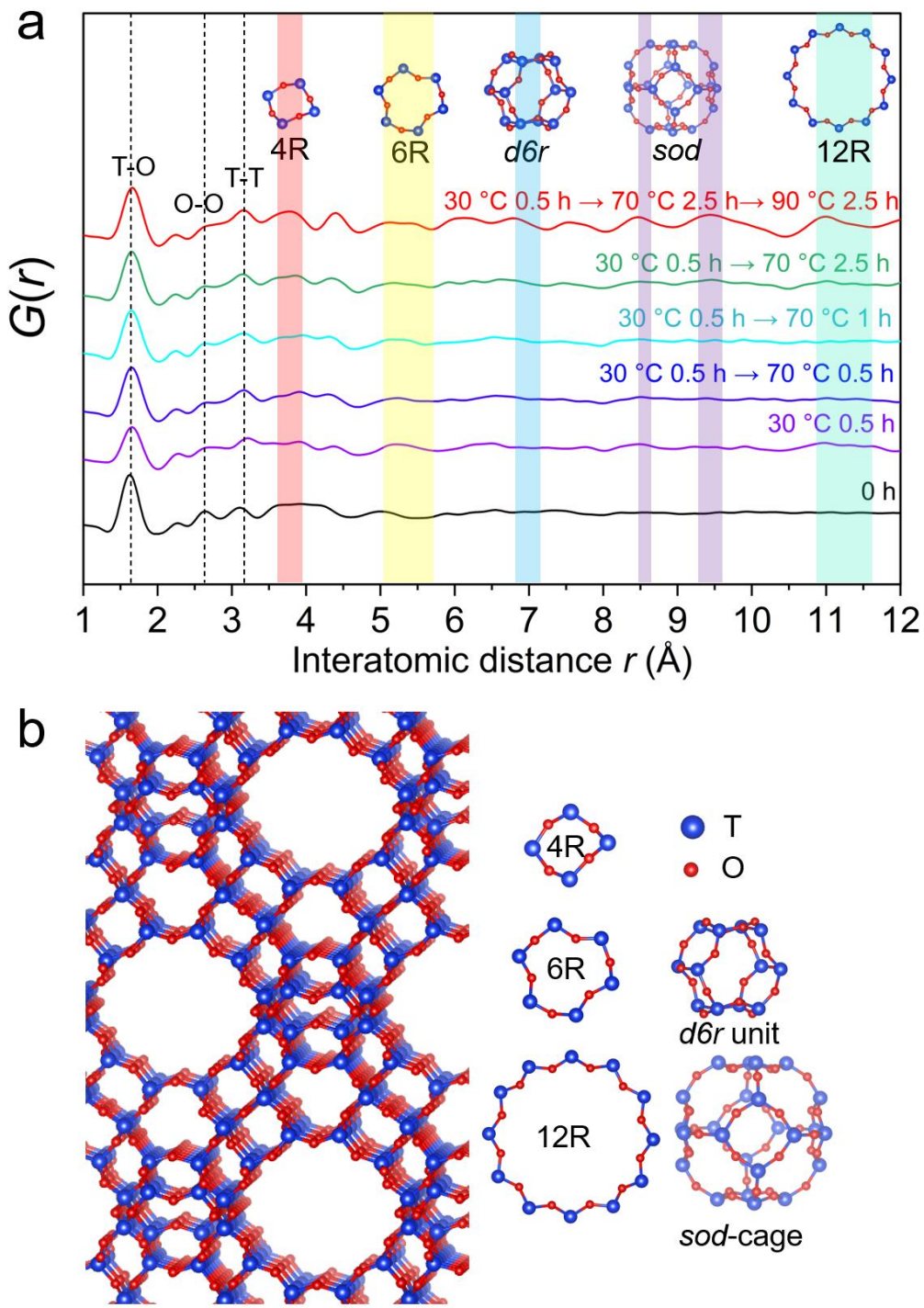

Fig. 3. (a) *Ex-situ* PDF patterns of the as-obtained solid products throughout the synthesis. (b) Illustration of the structural model of zeolite X.

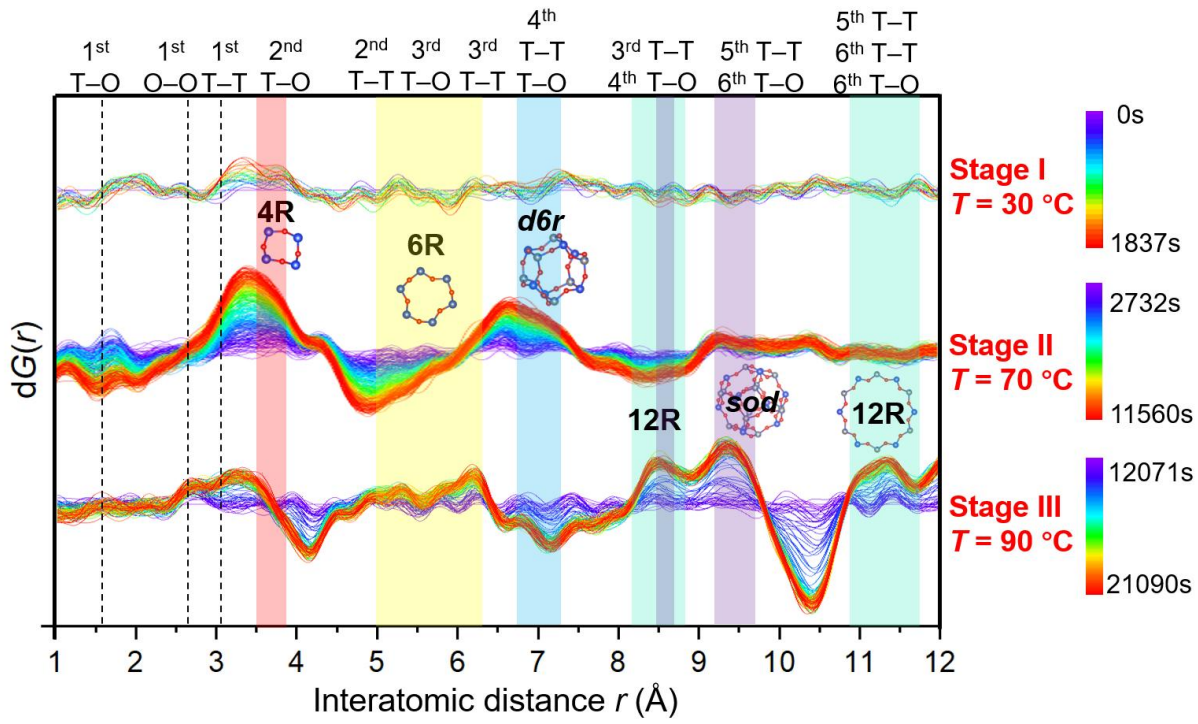

Fig. 4. Time-resolved relative PDF, d$G(r)$, of the reactant throughout the three stages of heating under the following conditions: (I) 30 °C for 30 min (0-1837 s). (II) 70 °C for 2.5 h (2732-11560 s). (III) 90 °C for 2.5 h (12071-21090 s). During stage (I) at 30 °C, there was no visible change in the local structure. During stage (II) at 70 °C, the increase in the 4Rs, decrease in the 6Rs, and the formation of *d6r* units are observed. During the final stage (III) at 90 °C, ordered large structures including 12Rs and *sod*-cages are formed.

Time-resolved PDF analysis based on the *in-situ* HEXTS measurement is a promising approach for investigating the structural evolutions in the disordered materials [30]. During the synthesis of zeolite X, a time-resolved pattern of total structure factor $S(Q)$ is shown in Fig. S3, and a time-resolved PDF is illustrated in Fig. S4. However, relative changes in the PDF with time are not significant enough to identify due to the abundance of water molecules in the reactant system. Therefore, relative PDFs, noted as d$G(r)$, are calculated to make the relative changes in local structures more discernible (Fig. 4). It is observed by *in-situ* high-energy XRD (HEXRD) that no diffraction peak is formed during the 30 °C and 70 °C stages (Fig. S5). Again, it can be confirmed that no zeolitic structure is formed before reaching the 90 °C stage. When the reactant mixture is agitated at 30 °C, there is no significant signal in the relative PDF pattern, suggesting that no obvious changes

in the local structure occur at this relatively low temperature. As the temperature increases to 70 °C, the peak at ca. 3.6 Å (T−O 2nd correlation in the 4Rs) is significantly enhanced, verifying the formation of ordered 4Rs, which is in accordance with the findings from the *ex-situ* PDF analysis. The increasingly pronounced band between 6.9 Å and 7.2 Å is assigned to the T−O 4th correlation in the *d6r* units, confirming the formation of *d6r* units before the diffraction peaks appear. Meanwhile, a reduction in the band of ca. 5.1–6.1 Å suggests that the 6Rs were initially abundant in the Si source but relatively decreased during the 70 °C-aging stage. During the hydrothermal treatment under 90 °C, the *d6r* units formed during the aging period decreased, and the appearance of three bands at ca. 8.6 Å, 9.5 Å and 11.4 Å are the exclusive fingerprints of the *sod*-cages and 12Rs, respectively. The 8.6 Å can be attributed to the T−O 4th correlation in the 12Rs as well as the T−O 5th correlation in the *sod*-cages. The peak at 9.5 Å is assigned to the T−O 6th correlation of *sod*-cages, and the peak centered at 11.4 Å is due to the T−T 5th correlation/ T−T 6th correlation in the 12Rs. The time when the large structures (12Rs, *sod*-cages) were formed and when the crystalline peaks appeared are comparatively demonstrated in Fig. S5. At 90 °C, the formation of 12Rs, *sod*-cages, and the appearance of crystalline peaks in the *in-situ* HEXRD pattern occurred simultaneously. The formation of *sod*-cages along with the ordered 12Rs might indicate the formation of a unit cell where several connected *sod*-cages collectively form a supercage at their center with 12R-openings. Commonly, a nucleus is defined as a stable and structurally-ordered cluster of atoms that serves as the basis for crystal growth [41]. Based on this definition, the formation of ordered large structures, including the largest rings (12Rs) and the well-defined *sod*-cages, can be considered as an important sign of the nucleation of zeolite X and possibly triggered the subsequent crystal growth.

4. DISCUSSION

Based on the *ex-situ* characterizations mentioned above, information regarding the changes in relative crystallinity, chemical composition, crystal morphology, as well as the formation of certain ring structures during the formation of zeolite X could be obtained. Elemental analysis showed that the incorporation of Al species into the solid matrix and the dissolution of Si species started from the beginning of the synthesis and was completed after 30 min at 70 °C (Fig. 1c), when a primary amorphous material was presumably formed.

From the change in relative crystallinity, it is clear that the formation of zeolite X crystal could only occur at the 90 °C stage, approximately between 1152 s and 2367 s (Fig. 1b, 1d, and S5). Using the current synthesis conditions, treating the precursor constantly at lower temperatures ranging from room temperature (22 °C) to 70 °C for ca. 18900 s (5 h 15 min) cannot produce zeolite X crystals (Fig. S6), suggesting that a sufficiently high temperature is critical to the crystallization. Furthermore, SOD-type zeolite rather than zeolite X was formed after treating the same precursor at 90 °C constantly for 5 h 15 min (Fig. S6), indicating that the aging stage is also essential to the zeolite X formation process. On a microscopic scale, *ex-situ* UV-Raman spectroscopy (Fig. 2a) provides insight into the formation of rings and structure units during the synthesis of zeolite X. No significant structural change was observed at 30 °C, while at 70 °C and 90 °C, the 4Rs continuously increased. *d6r* units could be observed by the end of the aging process and became more pronounced after the hydrothermal treatment. In addition, ^{27}Al MAS NMR spectra (Fig. 2b) confirm that all the Al atoms are tetrahedrally coordinated in the solid framework. It is further suggested by NMR spectra that the Si–O–Al structure is probably formed at 30 °C due to the incorporation of Al into the amorphous network, which might trigger the formation of Al-rich rings and the structural ordering process at the subsequent 70 °C stage. *Ex-situ* HEXTS measurements (Fig. 3) further confirmed the above findings from UV-Raman spectra. Additionally, the existence of 6Rs in the Si source and the formation of *sod*-cages and 12Rs during the crystallization process were detected by *ex-situ* HEXTS.

However, the above-mentioned *ex-situ* methods have some limitations. In UV-Raman spectroscopy, the broad and diffused Raman shift band involving a variety of rings makes it challenging to identify the ring structures at the amorphous stage. Moreover, as a limitation of the *ex-situ* approach, the recovery of the solid samples from the as-obtained mixture involves several procedures including quenching, washing, filtrating and drying, which might affect the original structures of the samples. Therefore, *in-situ* HEXTS characterization was conducted to further reveal the structural evolutions during the zeolite formation process. Results from *in-situ* HEXTS-PDF analysis confirmed the formation of 4Rs, 6Rs and *sod*-cages as demonstrated by *ex-situ* HEXTS and UV-Raman spectroscopy. Meanwhile, it is noteworthy that some structural changes were exclusively observed by the *in-situ* HEXTS method. According to the *in-situ* HEXTS-PDF results (Fig.

4), the formation of *d6r* units and the decrease of 6Rs during the aging stage at 70 °C were observed, which could not be detected by the *ex-situ* UV-Raman or HEXTS methods. Additionally, the formation of ordered large structures (12R and *sod*-cages) was clearly observed by *in-situ* HEXTS during the hydrothermal treatment at 90 °C between ca. 1152 s and 2367 s, simultaneous with the appearance of Bragg diffraction peaks (Fig. S5). The formation of such ordered large structure is considered to be linked to the formation of crystalline phase.

To further clarify the impact of temperature on the local structural evolutions during the zeolite synthesis, additional *in-situ* HEXTS measurements are conducted at a series of constant temperatures (22 °C/30 °C /50 °C/70 °C/90 °C) for ca. 18900 s (5 h 15 min). The increase in 4Rs is observed at all the temperatures (Fig. S7-S11), which may be related to the incorporation of Al in the amorphous framework to form ordered Al-rich 4Rs. The formation of *d6r* units is observed within the temperature range of 30 °C to 70 °C. At 30 °C and 50 °C, the formation of *d6r* units can be slightly observed, with durations of ca. 3966 s and ca. 3774 s, respectively (Fig. S8, S9). At 70 °C, the *d6r* units are continuously formed for ca. 11299 s, showing a significantly more active formation process compared to the ones at lower temperatures (Fig. S10). These findings indicate that a rational control of the aging temperature is crucial for the formation of *d6r* units. In addition, the temperature-controlled experiments showed that the large rings (12R) and structure units (*sod*-cages) could only form at a relatively high temperature of 90 °C (Fig. S11) and could not form at lower temperatures (Fig. S7-S10) with the current reactant system. This suggests that temperature probably favors the formation of certain structures, thus controlling the crystallization pathways. In addition to syntheses at various constant temperatures, gradient experiments were also performed by aging the same precursor at other temperatures (30 °C or 50 °C) for 2.5 h prior to the hydrothermal treatment at 90 °C for 2.5 h (30 °C: Fig. S12; 50 °C: Fig. S13). In both cases, pure zeolite X was not obtained; instead, the products consisted of a mixture of FAU and LTA phases, which is due to the insufficient formation of *d6r* units during the aging stage, as evidenced by *in-situ* HEXTS-PDF data (Fig. S12b, S13b). In particular, structural evolutions during the aging process at room temperature (ca. 22 °C) for up to 2.5 h were also investigated. Same as aging at 70 °C, the products remained amorphous throughout the process, as evidenced by PXRD patterns (Fig. S14a) and SEM

images (Fig. S15a-d). However, the incorporation of Al into the amorphous silica matrix was significantly slower at room temperature than at 70 °C (Fig. S16). Moreover, the formation of 4-membered rings (4Rs) appeared less pronounced, and no *d6r* units or larger ordered structures were formed at room temperature, as confirmed by both *ex-situ* HEXTS (Fig. S17a) and *in-situ* HEXTS results (Fig. S7, S10). The lack of *d6r* units could explain why pure zeolite X was not obtained when the aging was conducted at room-temperature. These results show direct evidence that the aging temperature has a significant impact on the synthesis outcomes by controlling the local structure evolutions during aging, especially the formation of *d6r* units.

Furthermore, to confirm the role of *d6r* units in the formation process of zeolite X, a control experiment is conducted using a potassium-free precursor (Fig. S18) at the same synthetic conditions, and sodalite (SOD-type framework) was crystallized instead of zeolite X. Similarly, *in-situ* HEXTS measurement is conducted to observe the whole synthesis process (70 °C: Fig. S19, 90 °C: Fig. S20). During the synthesis process, 4Rs and *sod*-cages are formed while the *d6r* units cannot be formed, resulting in the formation of an SOD-type framework without *d6r* units instead of the FAU-type. It has also been previously reported that K^+ cations may promote the formation of *d6r* units [42], and it is speculated that hydrated K^+ cations can facilitate the assembly of 4Rs in the precipitated aluminosilicate species to form *d6r* units [43]. Thus, it is indicated that *d6r* units play an essential role in the formation of the FAU-type framework.

By summarizing all the above-mentioned findings, a possible scheme for the formation of zeolite X is proposed (Fig. 5). During the first stage under 30 °C, no significant structural change could be observed, while the incorporation of Al and the release of Si atoms have started. At the second stage, namely the aging process under 70 °C, the incorporation of Al species is completed, resulting in the formation of ordered Al-rich 4Rs. It can be speculated that 4Rs and 6Rs are already abundant in this amorphous aluminosilicate network [29]. During the aging stage, 6Rs relatively decrease while 4Rs relatively increase in fraction. Simultaneously, a significant increase in the *d6r* units in the amorphous aluminosilicate matrix is observed. The *d6r* units are presumably formed through the reconstruction of the amorphous network via the cleavage and reconnection of bonds, playing an essential role in the subsequent formation of large structures such as 12Rs and *sod*-cages. Large rings (12Rs), however, cannot be formed throughout the aging treatment. As the temperature finally

reaches the hydrothermal stage of 90 °C, ordered 12Rs and *sod*-cages are formed while Bragg diffraction peaks appear, indicating the formation of a long-range order and the disorder-to-order transition. Meanwhile, the *d6r* units formed in the previous stage decrease, suggesting that *d6r* units are assembled to form ordered large structures including 12Rs and *sod*-cages, which possibly triggered the subsequent crystal growth of zeolite X. It is clear that the temperature plays a crucial role in the formation of ring structures and structural units during the formation of zeolite X.

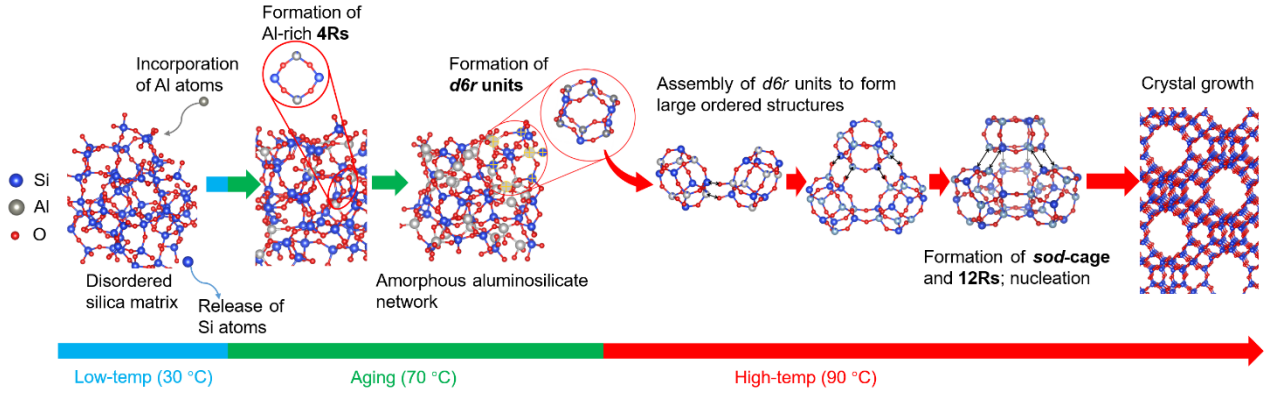

Fig. 5. Proposed scheme of the formation process of zeolite X (FAU). During the 30 °C stage and the early-70 °C stage, the incorporation of Al and release of Si atoms occurred. Then, during the aging stage at 70 °C, Al-rich 4Rs are formed as a result of the Al incorporation. As the relative fractions of 6Rs reduced, the *d6r* units were formed in the amorphous aluminosilicate network, which is presumably due to the reconstruction of the network via cleavage and reconnection of bonds. Finally, at a hydrothermal stage of 90 °C, ordered structures (12Rs and *sod*-cages) are formed by the assembly of the *d6r* units, evidencing the nucleation process and triggering the subsequent crystal growth.

Additionally, to investigate the impact of temperature on other types of zeolites, a supplementary experiment (Fig. S21) is conducted regarding the synthesis of zeolite A (LTA-type). The formation of 4Rs and 8Rs during the synthesis can be verified by UV-Raman spectroscopy (Fig. S22). Detailed structural evolutions are further investigated by the *in-situ* HEXTS measurements (Fig. S23, S24), and it is observed that large structures such as *d4r* units [44] and 8Rs could only be formed when the temperature is elevated to a higher level of 100 °C,

showing a similar model of local structural changes to that of zeolite X.

5. CONCLUSION

By combining a multi-step temperature profile with advanced *in-situ* HEXTS method and other characterization techniques, this work has clearly demonstrated the sequential formation of medium-range structures—rings (such as 4Rs), double rings (*d6r* and *d4r* units), and ordered large structures (8Rs, 12Rs and *sod*-cages)—at different temperatures. This approach allows a clear observation of the impact of temperature at different stages during the formation of zeolites. At an optimum aging temperature of 70 °C, an amorphous precursor rich in *d6r* units is formed, enabling the subsequent formation of ordered large structures (12Rs and *sod*-cages) at 90 °C, finally leading to the formation of the FAU-type zeolite framework. In comparison, direct hydrothermal treatment at 90 °C without aging at 70 °C results in the formation of untargeted SOD-type zeolite without *d6r* units. This work revealed the significant impact of temperature on the medium-range structure evolutions during the formation of zeolites, thus demonstrating that rational design and synthesis of zeolites can be achieved by a careful design of the temperature profile. This further opens up opportunities for the discovery of zeolites with novel structures and compositions, and the development of new synthesis routes for zeolites with wide applications in chemical industry.

ASSOCIATED CONTENT

Data Availability

All data needed to evaluate the conclusions in the paper are present in the paper and/or the Supplementary Materials. Additional data that support the findings of this study are available from the corresponding author upon reasonable request.

Supporting Information

Description of the homemade hydrothermal reactor system, experimental setting for the *in-situ* HEXTS measurement; synthesis time, relative crystallinity, composition, SEM images, and UV-Raman spectra of the

as-synthesized solid products; theoretical interatomic distances in the zeolite X framework; time-resolved total structure factor and time-resolved PDF pattern of the reactant system throughout the three stages of synthesis (30 °C, 70 °C, 90 °C) obtained by *in-situ* HEXTS measurement; selected HEXRD and relative PDF patterns during the three-stage synthesis; temperature profiles of the zeolite X precursors treated constantly at different temperatures (22 °C, 30 °C, 50 °C, 70 °C, 90 °C), HEXRD patterns and PXRD patterns of the as-obtained solid products after ca. 18900 s; time-resolved HEXRD patterns and relative PDF patterns measured during the constant treatment under the above temperatures; temperature profile of the synthesis from the potassium-free precursor, PXRD pattern of the product, time-resolved HEXRD patterns and relative PDF patterns; illustration of the structural model of zeolite A (LTA-type); temperature profile of the two-stage synthesis of zeolite A; PXRD pattern, SEM images, and UV-Raman spectra of the samples collected during the synthesis of zeolite A; time-resolved HEXRD patterns and relative PDF patterns measured during the synthesis of zeolite A

AUTHOR INFORMATION

Corresponding Author

Toru Wakihara − *Department of Chemical System Engineering, The University of Tokyo, Tokyo 113-8656, Japan; Institute of Engineering Innovation, The University of Tokyo, Tokyo 113-8656, Japan;* orcid.org/0000-0002-3916-3849; Phone: +81-3-5841-3821; Email: wakihara@chemsys.t.u-tokyo.ac.jp

Authors

Zimu Zhou − *Department of Chemical System Engineering, The University of Tokyo, Tokyo 113-8656, Japan;* orcid.org/0009-0009-6882-101X

Peidong Hu − *Department of Chemical System Engineering, The University of Tokyo, Tokyo 113-8656, Japan; Institute of Engineering Innovation, The University of Tokyo, Tokyo 113-8656, Japan*

Hiroki Yamada − *Japan Synchrotron Radiation Research Institute/SPring-8, Hyogo 679-5198, Japan; Faculty of Materials for Energy, Shimane University, 1060 Nishi-Kawatsu-Cho, Matsue, Shimane 690-8504, Japan*

Jochi Tseng − *Japan Synchrotron Radiation Research Institute/SPring-8, Hyogo 679-5198, Japan*

Koji Ohara − *Japan Synchrotron Radiation Research Institute/SPring-8, Hyogo 679-5198, Japan; Faculty of Materials for Energy, Shimane University, 1060 Nishi-Kawatsu-Cho, Matsue, Shimane 690-8504, Japan;* orcid.org/0000-0002-3134-512X

Yasuo Yonezawa − *Institute of Engineering Innovation, The University of Tokyo, Tokyo 113-8656, Japan*

Tatsuya Okubo − *Department of Chemical System Engineering, The University of Tokyo, Tokyo 113-8656, Japan;* orcid.org/0000-0002-1681-0193

Notes

The authors declare no competing interests.

ACKNOWLEDGEMENTS

This work was partly supported by New Energy and Industrial Technology Development Organization Moonshot Project; Japan Society for the Promotion of Science (JSPS) KAKENHI Grants-in-Aid for Scientific Research (S) (JP21H05011 and JP23H05454) and Transformative Research Areas (A) (JP20A206/20H05880); and Ministry of Education, Culture, Sports, Science and Technology (MEXT) "Establish Process Science toward Commercialization of Materials (Materialize)" Project (JPMXP0219192801). *In-situ* HEXTS measurements conducted at beamline 08W, SPring-8, Japan, were approved by Japan Synchrotron Radiation Research Institute under the proposal numbers 2021B1003, 2022A1207, 2022A1210, 2023A1367, 2023B1197, 2023B1199, and 2024A1225.

REFERENCES

(1) Davis, M. E.; Lobo, R. F. Zeolite and Molecular Sieve Synthesis. *Chem. Mater.* **1992**, *4*, 756–768.

(2) Li, Y.; Li, L.; Yu, J. Applications of Zeolites in Sustainable Chemistry. *Chem* **2017**, *3* (6), 928–949.

(3) Grand, J.; Awala, H.; Mintova, S. Mechanism of Zeolites Crystal Growth: New Findings and Open Questions. *CrystEngComm* **2016**, *18* (5), 650–664.

(4) Parmar, D.; Niu, Z.; Liang, Y.; Dai, H.; Rimer, J. D. Manipulation of Amorphous Precursors to Enhance

Zeolite Nucleation. *Faraday Discuss.* **2021**, *235*, 322–342.

(5) Cundy, C. S.; Cox, P. A. The Hydrothermal Synthesis of Zeolites: Precursors, Intermediates and Reaction Mechanism. *Microporous Mesoporous Mater.* **2005**, *82* (1–2), 1–78.

(6) Li, R.; Chawla, A.; Linares, N.; Sutjianto, J. G.; Chapman, K. W.; Martínez, J. G.; Rimer, J. D. Diverse Physical States of Amorphous Precursors in Zeolite Sol Gel Syntheses. *Ind. Eng. Chem. Res.* **2018**, *57* (25), 8460–8471.

(7) Kordala, N.; Wyszkowski, M. Zeolite Properties, Methods of Synthesis, and Selected Applications. *Molecules* **2024**, *29* (5), 1069.

(8) Mizuno, Y.; Miyake, K.; Tanaka, S.; Nishiyama, N.; Fukuhara, C.; Kong, C. Y. Phase-Controlled Synthesis of Zeolites from Sodium Aluminosilicate under OSDA/Solvent-Free Conditions. *Eur. J. Inorg. Chem.* **2021**, *2021* (14), 1405–1409.

(9) Aulia, D.; Culsum, N. T. U.; Kadja, G. T. M. Current Progress in the Synthesis of Zeolite Crystals at Low Temperatures and Their Catalytic Applications. *J. Nanopart. Res.* **2024**, *26* (5), 79.

(10) Borel, M.; Dodin, M.; Daou, T. J.; Bats, N.; Harbuzaru, B.; Patarin, J. SDA-Free Hydrothermal Synthesis of High-Silica Ultra-Nanosized Zeolite Y. *Cryst. Growth Des.* **2017**, *17* (3), 1173–1179.

(11) Park, M.; Han, S.; And, K.; Heo, N. H.; Komarneni, S. Synthesis of Zeolite Rho: Aging Temperature Effect. *J. Porous Mater.* **1996**, *3*, 151–155.

(12) Yoshioka, T.; Liu, Z.; Iyoki, K.; Chokkalingam, A.; Yonezawa, Y.; Hotta, Y.; Ohnishi, R.; Matsuo, T.; Yanaba, Y.; Ohara, K.; Takewaki, T.; Sano, T.; Okubo, T.; Wakihara, T. Ultrafast and Continuous-Flow Synthesis of AFX Zeolite via Interzeolite Conversion of FAU Zeolite. *React. Chem. Eng.* **2021**, *6* (1), 74–81.

(13) Cejka, J.; van Bekkum, H.; Corma, A.; Schüth, F., Eds. *Introduction to Zeolite Science and Practice*, 3rd ed.; Elsevier: Amsterdam, 2007.

(14) Asgar Pour, Z.; Alassmy, Y. A.; Sebakhy, K. O. A Survey on Zeolite Synthesis and the Crystallization Process: Mechanism of Nucleation and Growth Steps. *Crystals (Basel)* **2023**, *13* (6), 959.

(15) Houlleberghs, M.; Breynaert, E.; Asselman, K.; Vaneeckhaute, E.; Radhakrishnan, S.; Anderson, M.

W.; Taulelle, F.; Haouas, M.; Martens, J. A.; Kirschhock, C. E. A. Evolution of the Crystal Growth Mechanism of Zeolite W (MER) with Temperature. *Microporous Mesoporous Mater.* **2019**, *274*, 379–384.

(16) Drewitt, J. W. E.; Hennet, L.; Neuville, D. R. From Short to Medium Range Order in Glasses and Melts by Diffraction and Raman Spectroscopy. *Rev. Mineral. Geochem.* **2022**, *87*, 55–103.

(17) Fengtao, F.; Zhaochi, F.; Can, L. UV Raman Spectroscopic Study on the Synthesis Mechanism and Assembly of Molecular Sieves. *Chem. Soc. Rev.* **2010**, *39* (12), 4794–4801.

(18) Yu, Y.; Xiong, G.; Li, C.; Xiao, F.-S. Characterization of Aluminosilicate Zeolites by UV Raman Spectroscopy. *Microporous Mesoporous Mater.* **2001**, *46*, 23–34.

(19) Chen, C. T.; Iyoki, K.; Yonezawa, Y.; Okubo, T.; Wakihara, T. Understanding the Nucleation and Crystal Growth of Zeolites: A Case Study on the Crystallization of ZSM-5 from a Hydrogel System under Ultrasonication. *J. Phys. Chem. C* **2020**, *124* (21), 11516–11524.

(20) Dib, E.; Clatworthy, E. B.; Lakiss, L.; Ruaux, V.; Mintova, S. Hydroxyl Environments in Zeolites Probed by Deuterium Solid-State MAS NMR Combined with IR Spectroscopy. *Inorg. Chem. Front.* **2022**, *9* (12), 2964–2968.

(21) Terban, M. W.; Billinge, S. J. L. Structural Analysis of Molecular Materials Using the Pair Distribution Function. *Chem. Rev.* **2022**, *122* (1), 1208–1272.

(22) Hikichi, N.; Iyoki, K.; Naraki, Y.; Yanaba, Y.; Ohara, K.; Okubo, T.; Wakihara, T. Role of Sodium Cation during Aging Process in the Synthesis of LEV-Type Zeolite. *Microporous Mesoporous Mater.* **2019**, *284*, 82–89.

(23) Hu, P.; Iyoki, K.; Yamada, H.; Yanaba, Y.; Ohara, K.; Katada, N.; Wakihara, T. Synthesis and Characterization of MFI-Type Zincosilicate Zeolites with High Zinc Content Using Mechanochemically Treated Si–Zn Oxide Composite. *Microporous Mesoporous Mater.* **2019**, *288*, 109594.

(24) Hikichi, N.; Iyoki, K.; Yanaba, Y.; Ohara, K.; Okubo, T.; Wakihara, T. Superior Ion-Exchange Property of Amorphous Aluminosilicates Prepared by a Co-Precipitation Method. *Chem. Asian J.* **2020**, *15* (13),

2029–2034.

(25) Yamada, H.; Sukenaga, S.; Ohara, K.; Anand, C.; Ando, M.; Shibata, H.; Okubo, T.; Wakihara, T. Comparative Study of Aluminosilicate Glass and Zeolite Precursors in Terms of Na Environment and Network Structure. *Microporous Mesoporous Mater.* **2018**, *271*, 33–40.

(26) Peng, C.; Liu, Z.; Horimoto, A.; Anand, C.; Yamada, H.; Ohara, K.; Sukenaga, S.; Ando, M.; Shibata, H.; Takewaki, T.; Mukti, R. R.; Okubo, T.; Wakihara, T. Preparation of Nanosized SSZ-13 Zeolite with Enhanced Hydrothermal Stability by a Two-Stage Synthetic Method. *Microporous Mesoporous Mater.* **2018**, *255*, 192–199.

(27) Kohara, S.; Suzuya, K. High-Energy X-Ray Diffraction Studies of Disordered Materials. *Nucl. Instrum. Methods Phys. Res., B* **2003**, *199*, 23–28.

(28) Yamada, H.; Horikawa, H.; Anand, C.; Ohara, K.; Ina, T.; Machida, A.; Tominaka, S.; Okubo, T.; Liu, Z.; Iyoki, K.; Wakihara, T. Atom-Selective Analyses Reveal the Structure-Directing Effect of Cs Cation on the Synthesis of Zeolites. *J. Phys. Chem. Lett.* **2023**, *14* (14), 3574–3580.

(29) Wakihara, T.; Kohara, S.; Sankar, G.; Saito, S.; Sanchez-Sanchez, M.; Overweg, A. R.; Fan, W.; Ogura, M.; Okubo, T. A New Approach to the Determination of Atomic-Architecture of Amorphous Zeolite Precursors by High-Energy X-Ray Diffraction Technique. *Phys. Chem. Chem. Phys.* **2005**, *8* (2), 224–227.

(30) Chen, C. T.; Iyoki, K.; Hu, P.; Yamada, H.; Ohara, K.; Sukenaga, S.; Ando, M.; Shibata, H.; Okubo, T.; Wakihara, T. Reaction Kinetics Regulated Formation of Short-Range Order in an Amorphous Matrix during Zeolite Crystallization. *J. Am. Chem. Soc.* **2021**, *143* (29), 10986–10997.

(31) Ohara, K.; Tominaka, S.; Yamada, H.; Takahashi, M.; Yamaguchi, H.; Utsuno, F.; Umeki, T.; Yao, A.; Nakada, K.; Takemoto, M.; Hiroi, S.; Tsuji, N.; Wakihara, T. Time-Resolved Pair Distribution Function Analysis of Disordered Materials on Beamlines BL04B2 and BL08W at SPring-8. *J. Synchrotron Radiat.* **2018**, *25* (6), 1627–1633.

(32) Minami, A.; Hu, P.; Sada, Y.; Yamada, H.; Ohara, K.; Yonezawa, Y.; Sasaki, Y.; Yanaba, Y.; Takemoto, M.; Yoshida, Y.; Okubo, T.; Wakihara, T. Tracking Sub-Nano-Scale Structural Evolution in Zeolite

Synthesis by in Situ High-Energy X-Ray Total Scattering Measurement with Pair Distribution Function Analysis. *J. Am. Chem. Soc.* **2022**, *144*, 23313–23320.

(33) Wakihara, T.; Sato, K.; Sato, K.; Tatami, J.; Kohara, S.; Komeya, K.; Meguro, T. Preparation of Nano-Zeolite X by Bead-Milling and Post-Milling Recrystallization. *J. Ceram. Soc. Jpn.* **2012**, *120* (8), 341–343.

(34) Johnson, E. B. G.; Arshad, S. E. Hydrothermally Synthesized Zeolites Based on Kaolinite: A Review. *Appl. Clay Sci.* **2014**, *97–98*, 215–221.

(35) Ogura, M.; Kawazu, Y.; Takahashi, H.; Okubo, T. Aluminosilicate Species in the Hydrogel Phase Formed during the Aging Process for the Crystallization of FAU Zeolite. *Chem. Mater.* **2003**, *15* (13), 2661–2667.

(36) Tominaka, S.; Yamada, H.; Hiroi, S.; Kawaguchi, S. I.; Ohara, K. Lepidocrocite-Type Titanate Formation from Isostructural Prestructures under Hydrothermal Reactions: Observation by Synchrotron X-Ray Total Scattering Analyses. *ACS Omega* **2018**, *3* (8), 8874–8881.

(37) Khouchaf, L.; Boulahya, K.; Das, P. P.; Nicolopoulos, S.; Kis, V. K.; Lábár, J. L. Study of the Microstructure of Amorphous Silica Nanostructures Using High-Resolution Electron Microscopy, Electron Energy Loss Spectroscopy, X-Ray Powder Diffraction, and Electron Pair Distribution Function. *Materials* **2020**, *13* (19), 1–14.

(38) Knops-Gerrits, P.-P.; De Vos, D. E.; Feijen, E. J. P.; Jacobs, P. A. Raman Spectroscopy on Zeolites. *Microporous Mesoporous Mater.* **1997**, *8*, 3–17.

(39) Wakihara, T.; Saito, Y.; Tatami, J.; Komeya, K.; Meguro, T.; Mackenzie, K. J. D.; Takagi, S.; Yokouchi, M. NMR Study on the Formation Mechanism of β-SiAlON from Zeolite by Nitridation Using Ammonia Gas. *J. Ceram. Soc. Jpn.* **2008**, *116*, 980–983.

(40) Farrow, C. L.; Juhas, P.; Liu, J. W.; Bryndin, D.; Boin, E. S.; Bloch, J.; Proffen, T.; Billinge, S. J. L. PDFfit2 and PDFgui: Computer Programs for Studying Nanostructure in Crystals. *J. Condens. Matter Phys.* **2007**, *19* (33), 335219.

(41) Kasahara, S.; Itabashi, K.; Igawa, K. Clear Aqueous Nuclei Solution for Faujasite Synthesis. *Stud. Surf.*

Sci. Catal. **1986**, *28*, 185–192.

(42) Kadja, G. T. M.; Kadir, I. R.; Fajar, A. T. N.; Suendo, V.; Mukti, R. R. Revisiting the Seed-Assisted Synthesis of Zeolites without Organic Structure-Directing Agents: Insights from the CHA Case. *RSC Adv.* **2020**, *10* (9), 5304–5315.

(43) Iwama, M.; Suzuki, Y.; Plévert, J.; Itabashi, K.; Ogura, M.; Okubo, T. Location of Alkali Ions and Their Relevance to Crystallization of Low Silica X Zeolite. *Cryst. Growth Des.* **2010**, *10* (8), 3471–3479.

(44) Dutta, P. K.; Barco, B. Del. Raman Spectroscopy of Zeolite A: Influence of Si/AI Ratio. *J. Phys. Chem.* **1988**, *92*, 354–357.

Table of Contents